PAPER

Drag reduction on laser-patterned hierarchical superhydrophobic surfaces†

K. M. Tanvir Ahmmed and Anne-Marie Kietzig*

Hierarchical laser-patterned surfaces were tested for their drag reduction abilities. A tertiary level of surface roughness which supports stable Cassie wetting was achieved on the patterned copper samples by laser-scanning multiple times. The laser-fabricated micro/nano structures sustained the shear stress in liquid flow. A rheometer setup was used to measure the drag reduction abilities in term of slip lengths on eight different samples. A considerable increase in slip length (111% on a grate sample) was observed on these surfaces compared to the slip length predictions from the theoretical and the experimental models for the non-hierarchical surfaces. The increase in slip lengths was correlated to the secondary level of roughness observed on the patterned samples. The drag reduction abilities of three different arrangements of the surface features were also compared: posts in a square lattice, parallel grates, and posts in a hexagonal lattice. Although the latter facilitates a stable Cassie state, it nevertheless resulted in a lower normalized slip length compared to the other two arrangements at a similar solid fraction. Furthermore, we coated the laser-patterned surfaces with a silane to test the effect of surface chemistry on drag reduction. While the contact angles were surprisingly similar for both the non-silanized and the silanized samples, we observed higher slip lengths on the latter, which we were able to explain by measuring the respective penetration depths of the liquid–vapour interface between surface features.

1. Introduction

Drag reduction is beneficial for almost all fluid flow applications. Various active and passive techniques, such as riblets, coatings, and air bubble injection have been developed over the years to reduce drag in fluid flow. However, the drag reduction ability of superhydrophobic surfaces has garnered more attention, and it has been extensively studied in the past decade.[1–4] A superhydrophobic surface has a high apparent contact angle, a small contact angle hysteresis (the difference between the advancing and the receding contact angles) and high stability in the Cassie state of wetting.[5] Superhydrophobic surfaces are characterized by both the chemical hydrophobicity and the surface roughness. Water droplets easily roll over superhydrophobic surfaces as the water interface is supported on roughness peaks and trapped air pockets. The relative fraction of the surface in contact with water is termed as the solid fraction. This solid fraction can be calculated from the well-known Cassie–Baxter equation if the Young's contact angle of the material is known. For a surface with a specific geometric pattern, the solid fraction

is often estimated as the top surface of the surface structure.[6] Drag reduction on superhydrophobic surfaces is achieved by reducing the solid fraction. Thus, the no-slip boundary condition is not an appropriate boundary condition on a superhydrophobic surface but is better replaced by a slip boundary condition on these surfaces. The slip boundary condition proposed by Navier (1823) states that the slip velocity at a solid wall is proportional to the shear rate experienced by the fluid at the wall; thus, $v_w = b_{slip}\gamma_w$, where v_w is the velocity at the wall, b_{slip} is the slip length, and γ_w is the shear rate at the wall.[7] However, on a smooth hydrophobic surface, the amount of slip is negligible in most normal flow conditions because of the absence of air trapping. The intrinsic slip length on a hydrophobic surface varies from nanometers to a few microns,[8,9] whereas to the best of our knowledge the highest reported slip length on a superhydrophobic surface is 400 µm.[10] The measured slip length on a superhydrophobic surface is the effective slip length for the surface having both the shear-free air–water interface between the roughness valleys and the no-slip solid–water contact on roughness peaks. For liquid flow past a superhydrophobic surface, a large effective slip length results in a high drag reduction.

The effective slip length of a superhydrophobic surface depends on various parameters. According to the scaling analysis by Ybert *et al.* (2007), there are to name the surface feature sizes, the arrangements of the features, and the solid fraction of the surface.[6] Drag reduction on superhydrophobic surfaces has only been

Department of Chemical Engineering, McGill University, Montréal, Quebéc, Canada.
E-mail: anne.kietzig@mcgill.ca

† Electronic supplementary information (ESI) available: Confocal microscopy 3D profile and height profile, slip length variation with shear rate, overall mean and mean slip length, slip lengths on silanized and non-silanized samples, cross-sectional height profiles of a sample. See DOI: 10.1039/c6sm00436a

investigated in few geometries and arrangements. Many studies experimentally investigated drag reduction on square pillars,[11] cylindrical posts,[12,13] parallel grates,[14–16] transverse grates,[17,18] mesh samples[19] and hole structures.[20,21] Drag reduction was also observed on nano-textured[22–24] and random rough surfaces.[25] One of the important arrangements, the hexagonal arrangement, was not studied extensively. The hexagonal arrangements promote a stable Cassie wetting state, as the surface features are equidistant from each other and in closest proximity. The only known work of such kind by Bixler and Bhushan (2014) studied the fluid flow on comparatively short posts in a hexagonal arrangement.[26] However, this study was not conclusive. Thus, a comparison among different arrangements, that include the hexagonal arrangement, is outstanding.

Parameters other than the feature size, shape, and arrangement can also affect the effective slip lengths. One such parameter is the dual-scale roughness of a superhydrophobic surface. Dual-scale roughness is not a necessary condition for a surface to be superhydrophobic. However, many naturally occurring super-hydrophobic surfaces, so-called hierarchical surfaces, have dual-scale roughness. The hierarchical roughness increases the slip length because the secondary roughness acts as an intrinsic slip surface on top of the primary feature. A study by Jung and Bhushan (2010) on a hierarchical superhydrophobic surface has shown increased slip length compared to a non-hierarchical superhydrophobic surface with an identical primary feature size.[12] In contrast, in a different study by Lee and Kim (2011), both increased and decreased slip lengths were observed for hierarchical surfaces with different solid fractions.[27] The decrease in slip lengths for certain hierarchical surfaces with low solid fractions was attributed to the partial penetration of the solid–air–water interface into the surface microstructures. Thus, the beneficial effect of the hierarchical structures was lost on those surfaces. Therefore, at a low solid fraction, without experimentation, it is difficult to predict whether an additional scale of roughness will result in increased drag reduction. Furthermore, only post structures were used in previous experimental studies to measure the effect of hierarchical features on drag reduction.

In addition to the surface parameters, the methods of fabricating superhydrophobic surfaces need to be considered to effectively apply these surfaces in industrial applications. The first drag reduction studies on superhydrophobic surfaces focused only on laminar flow. However, recent works showed that drag reduction on superhydrophobic surfaces was also achieved in turbulent flow.[15,18,28] Moreover, 50% drag reduction was reported for a large flat plate of 0.74 m^2 at a Reynolds number of 3.7×10^5.[29] Such results lead us closer to effective large-scale industrial applications of superhydrophobic surfaces, beyond their current use in microfluidic devices. The possible large-scale uses are in biomedical devices, pipe flow systems and underwater vehicle operation. However, most of the processes, such as photolithography and chemical vapour deposition, used to fabricate test surfaces for fundamental research experiments are not easily scalable and require several process steps. Femtosecond laser micromachining, unlike most other processes, can fabricate large-scale superhydrophobic surfaces in an easy one-step process on all types of materials ranging from metals to polymers. Although, the fabrication of superhydrophobic surfaces by femtosecond laser micromachining has received much attention in recent years,[30,31] to the best of our knowledge, slip on these surfaces has not yet been investigated.

In this study, we fabricated hierarchical superhydrophobic surfaces by a single-step laser micromachining process and tested them in continuous liquid flow using a rheometer. More precisely, for the first time we compared the drag reduction abilities of parallel grates, as the simplest form of surface pattern, with rectangular and rhombic posts arranged in a square and hexagonal lattice, respectively. The hierarchical nature of the surfaces increased the slip lengths considerably compared to theoretical predictions and previous results on non-hierarchical surfaces. Furthermore, we investigated the effect of surface chemistry on drag reduction by patterned superhydrophobic surfaces and observed higher slip lengths on silane-coated surfaces compared to non-coated surfaces.

2. Experimental

2.1 Laser micromachining

Laser-patterned surfaces were fabricated on copper (99.9% purity, McMaster-Carr). The copper samples were polished with 600 and 1200 grit silicon carbide sandpaper prior to patterning. We used an amplified Ti:sapphire laser system (Coherent Libra) with <85 fs pulse duration, 800 nm wavelength, and 10 kHz repetition rate to produce a linearly polarized Gaussian beam. The beam was focused on the sample with a 100 mm plano-convex lens. The $1/e^2$ theoretical beam diameter at the focal plane was 22 μm. The sample was positioned 1 mm beyond the focal plane on a computer-controlled xyz translation stage (Newport Corporation). The patterning was carried out by translating the stage with velocities of 2 and 4 mm s^{-1} under the stationary laser beam. The GOL3D software (GBC&S) controlled stage translation and shutter (Uniblitz) opening. A computer-controlled variable attenuator, composed of a half-wave plate and a polarizing beam splitter, reduced the laser power from 4 W to 800 mW.

Eight samples of different feature patterns and different characteristic dimensions were fabricated by laser micro-machining. Four of those were designed with the primary feature being rectangular posts arranged in a square pattern, whereas two of them were designed as rhombic posts arranged in a hexagonal pattern. The remaining two samples show parallel grates. All samples were scanned five times. Samples with rectangular posts arranged in a square lattice are denoted by P1, P2, P3 and P4, whereas samples with rhombic posts arranged in a hexagonal lattice are labelled with P5H and P6H. Parallel grate samples arranged in the direction of flow are named as Gr1 and Gr2. P1, P3, P5H, and Gr1 samples were fabricated with a stage velocity of 4 mm s^{-1}, whereas other samples were fabricated with 2 mm s^{-1} stage velocity. The time needed to texture a sample varied for different patterned

samples. For example, it took ∼5 minutes to pattern 1 cm² area for Gr1 sample in a single scan. However, note that the process is scalable. Several micromachining parameters, such as scanning speed and power, can be modified simultaneously to pattern the surface faster. The laser micromachining process was carried out in air. Samples were cleaned with acetone in an ultrasonic bath before and after laser micromachining for ten minutes.

2.2 Surface modification

The ultrasonically cleaned samples were placed into a CO_2 chamber overnight at 20 psi pressure and 60 °C temperature. These samples were directly used in the slip length measurements. After testing these samples with a rheometer, they were coated with a fluoroalkylsilane ($1H,1H,2H,2H$-perfluorooctyltriethoxysilane, Sigma-Aldrich) using a dip-coating method. The samples were ultrasonically cleaned in acetone before starting the coating procedure. The silane solution was prepared by mixing methanol (90% v/v), water (6% v/v), and silane (4% v/v). We dipped the patterned samples into 0.1 M HCl solution for 1 minute and then rinsed them with reverse osmosis (RO) water to remove any excess amount of the solution. Afterwards, the samples were immersed into the silane solution and sonicated for one hour before being rinsed with methanol and placed in an oven overnight for curing at 100 °C.

2.3 Surface analysis

The resulting surface topographies were imaged by scanning electron microscopy (SEM) (FEI Inspect F50). The geometrical parameters of the patterned surfaces were measured with a 3D confocal microscope (Olympus LEXT OLS4000) in reflectance mode. The feature sizes were measured at longitudinal and transverse cross sections of the pillars. Four measurements were carried out for each cross section. An example of such cross section measurement is shown for sample P6H in ESI,† Fig. S1.

The dynamic (advancing and receding) contact angles were measured at room temperature with a goniometer (Data Physics OCA 15EC). An initial droplet size of 5 μL (filtered RO water) was used in the measurements. The droplet size was increased from 5 μL to 10 μL with a dispense rate of 0.1 μL s⁻¹ and then reduced back to 5 μL at the same rate for dynamic contact angle measurements. The contact angle measurements were repeated three times for each sample.

2.4 Slip length measurement

A rheometer (Anton Paar MCR302) was used to quantify the slip lengths, which were calculated by measuring torques. The operational torque of the instrument was between 0.01 μN m and 200 mN m with a torque resolution of 0.1 nN m. A cone-and-plate arrangement was used with RO water as the working liquid. The cone has a diameter of 25 mm, cone angle of 2°, and cone truncation of 103 μm, which results in a cone-plate distance of 0.44 μm at the periphery. The temperature of the bottom plate was held constant at 20 °C by a Peltier plate. The samples were mounted on the bottom plate, and four measurements were taken on each sample. Torques were measured at different shear rates ranging from 70 s⁻¹ to 150 s⁻¹. An equation

relating the torque and the effective slip length is necessary to calculate the latter at a fixed shear rate. The effective slip length and the effective slip velocity, by definition, are the area-averaged quantities. Thus, the shear rate is uniform on a superhydrophobic surface in a cone-and-plate rheometer system. The following equation is derived for Couette flow in a cone-and-plate rheometer system by solving the Navier–Stokes equations in spherical coordinates with Navier's slip boundary condition:[32]

$$M = \frac{2\pi\mu\omega R^3}{3\theta_0}\left(1 - \frac{3\delta}{2R\theta_0} + \frac{3\delta^2}{R^2\theta_0^2}\right) - 2\pi\mu\omega\frac{\delta^3}{\theta_0^4}\ln\left(\frac{R\theta_0 + \delta}{\delta}\right)$$

(1)

where M is the torque (N m), μ is the viscosity at 20 °C (Pa s), ω is the angular velocity of the cone (rad s⁻¹), R is the radius of the cone (m), θ_0 is the cone angle (rad), and δ is the effective slip length (m). A numerical method (using MATLAB®) was employed to find the slip length.

2.5 Air–water interface profiling

A confocal laser scanning microscope (Zeiss LSM 710) was employed to acquire a 3D-topography of an air–water interface under static condition on the patterned surfaces. A 63× water immersion lens (Zeiss W Plan-Apochromat) was used to obtain the depth profile. ImageJ® software was used to stack the images. A fixed amount of water (50 μL) was deposited on the immersion lens for all the measurements. Afterwards, the lens was moved down towards the sample until the sample was at focus. The measurements on different samples were acquired at the same vertical position of the lens. Thus, equal pressure was maintained on all the samples.

2.6 Robustness test

We submerged all samples under 40 cm of water (∼4 kPa of pressure) in a tall graduated cylinder to test for wetting robustness in a static condition. In addition, a horizontal rectangular flow channel was used to test the effect of surface chemistry on the robustness of the patterned surfaces in dynamic condition. The channel was fabricated from an impact-resistant polycarbonate slab. One side of the channel wall is replaceable with the patterned surface. After positioning the channel wall, the channel was watertight. The width of the channel is 10 mm, and the height is 1 mm. The channel is 300 mm in length, and the patterned section of 40 mm was machined at a distance of 215 mm from the entrance of the channel, thus eliminating the entrance effect. RO water was used as the working fluid. The water was driven by a gas pressure system. A tank filled with water was connected to a high-pressure N_2 gas cylinder. The flow rate was controlled by both the gas pressure and a needle valve installed in the flow line. The flow rate was measured with a paddle wheel flow meter (FTB 331D, Omega) and the meter was calibrated before the test. The flow rate used in these experiments was 122 mL min⁻¹, which corresponds to a Reynolds number of 368, thus, the flow was laminar. The temperature of the water was constant at 18 °C and monitored with a thermocouple.

3. Results and discussion

3.1 Surface features and feature arrangements

All samples were patterned by creating laser-inscribed lines with a multiple scan scheme. By comparing the lines inscribed by a single scan (Fig. 1(a)) to the multiple scans (Fig. 1(b)–(d)), we observed that multiple scans provided two benefits. Firstly, the lines became deeper with successive scanning (Fig. 1(e) and (f)). Secondly, microstructures formed at the periphery of the line (Fig. 1(a)–(d)). We reported previously the existence of the microstructures at the periphery of a multiple-scanned line without further investigation.[33] However, in this work we studied the effect of multiple scans on microstructure formation, as this formation was responsible for the hierarchical structures on the patterned samples. Fig. 1 clearly shows that (i) the size of the microstructures grew with increasing number of scans and (ii) the microstructures formed outside of the effective beam diameter (ω_{eff}). The effective beam diameter is defined as the experimentally observed line width resulting from a single laser scan at specific machining parameters (fluence, stage velocity and sample position) for a material machined in a defined environment.[34]

The simplest patterns created by the multiple-scanned laser-inscribed lines were the parallel grate samples: Gr1 and Gr2 (Fig. 2(a) and (b), respectively). Our laser micromachined samples have a tertiary level of surface roughness, as shown exemplarily for the Gr1 sample in Fig. 2(c) and (d). The laser-inscribed primary features are superimposed with micro-scale features, which add a secondary level of roughness (Fig. 2(c)). These micro-scale features are columnar in shape and thus will be referred to as micro-columns in this article. The micro-columns are composed of sub-microstructures (length scale of several hundred nanometers), which constitute the tertiary level of roughness. These sub-microstructures consist of laser-induced-periodic-surface-structures (LIPSS) and clustered nanoparticles (Fig. 2(d)). Moreover, the sidewalls of the primary features are decorated with LIPSS and nanoparticles. The presence of hierarchical features on a line inscribed by a laser beam is well known.[35,36] However, at the periphery of the line, the hierarchical features are typically limited to LIPSS and nanoparticles. In contrast, overscanning lines with the laser beam, as performed here, produces tall secondary microfeatures with a height of up to 15 μm (Fig. S1 in the ESI†).

Similarly, we achieved hierarchical features on all the post samples by using multiple laser scans. The four different types of rectangular post structures are shown in Fig. 3, whereas Fig. 4 shows the two samples with rhombic posts arranged in a hexagonal lattice. The rectangular post structures have two characteristic dimensions, lengths, and widths. Similarly, the rhombic posts have two characteristic dimensions: the two diagonals. In this work, we chose to place the rhombic posts in a hexagonal arrangement for two reasons. Firstly, a hexagonal arrangement is symmetric as the distance between neighbouring features are equal. Secondly, a hexagonal arrangement ensures the closest packing in an arrangement with the highest coordination number (number of neighbouring features) of six.
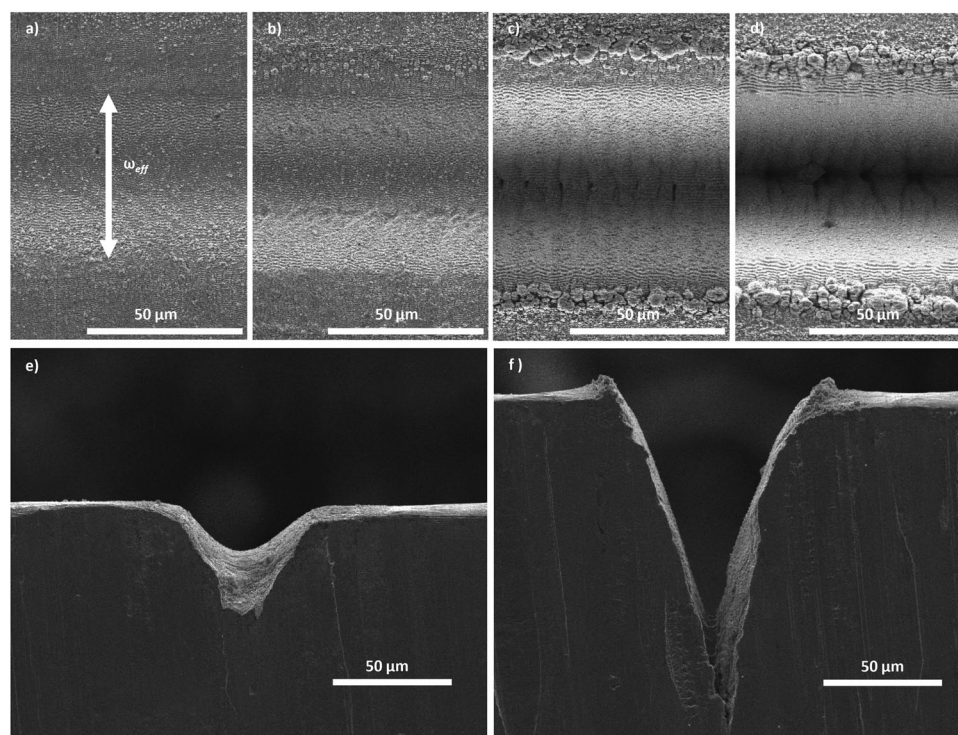

Fig. 1 Scanning electron microscopy (SEM) images of a laser inscribed line with: (a) a single scan, (b) double scans, (c) five scans, and (d) ten scans. SEM images of the cross sections of the line with: (e) double scans, and (f) ten scans. All lines were inscribed with a 4 mm s^{-1} stage velocity and 800 mW average laser power. The effective beam diameter is shown in (a).
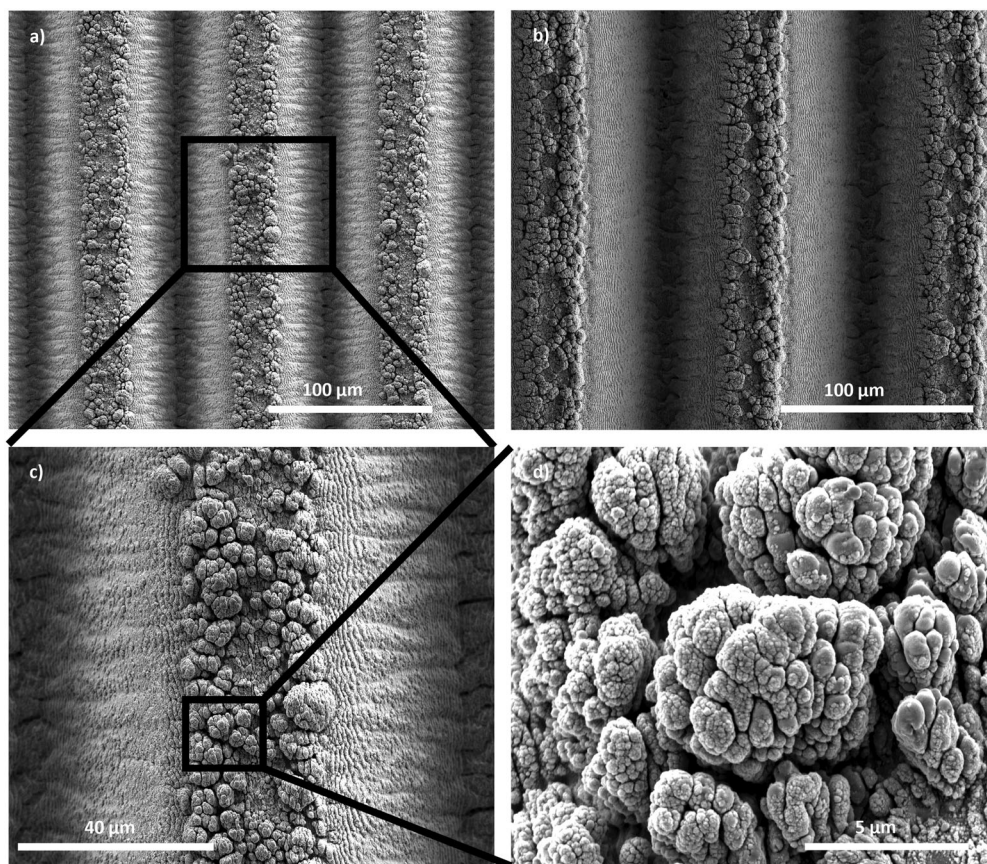
Fig. 2 Scanning electron microscopy (SEM) images for parallel grate structures: (a) sample Gr1, (b) sample Gr2, (c) and (d) magnified view of sample Gr1 showing the tertiary level of roughness.
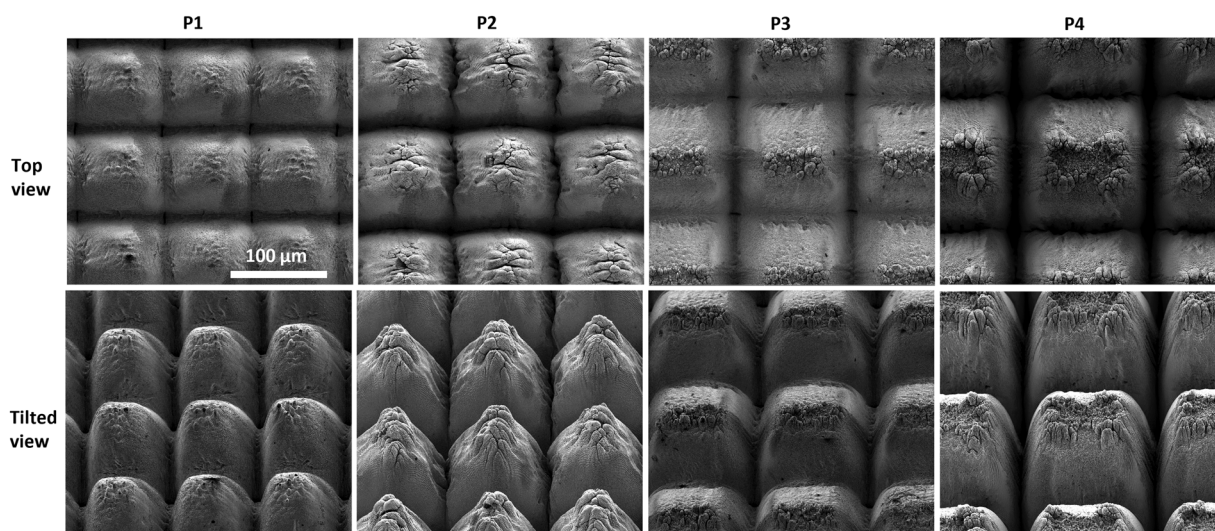

Fig. 3 Scanning electron microscopy (SEM) images for rectangular post structures. P1, P2, P3, and P4 samples (left to right) at normal view, and 30° tilted view. The posts are arranged in a square lattice. The scale bar applies to all images.

Sufficiently dense posts in the hexagonal arrangement assure the Cassie state of wetting.[37]

The number of scans is one of the important parameters for creating the hierarchical features shown in Fig. 2–4. The effect of multiple scans on laser-inscribed surface structures observed in this study is entirely different from that of the laser-induced surface structures produced by multiple scans reported elsewhere.[38] In the latter case, the surface structures grew at random
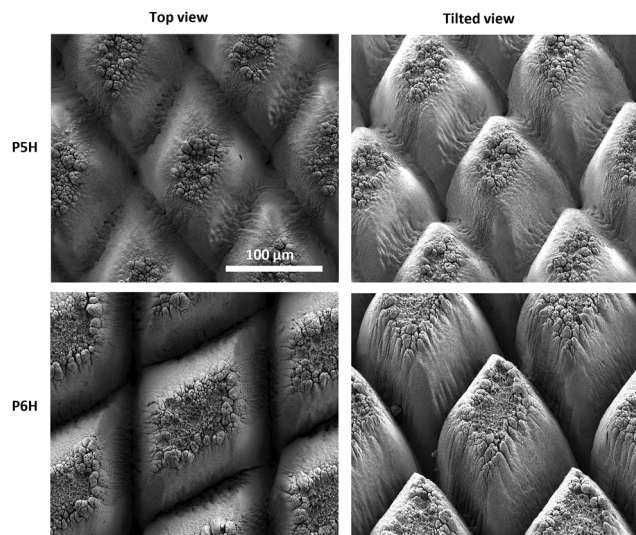
Fig. 4 Scanning electron microscopy (SEM) images for rhombic post structures. P5H, and P6H samples (top to bottom) at normal view, and 30° tilted view. The posts are arranged in a regular hexagonal lattice. The scale bar applies to all images.

Table 1 Characteristic dimensions and feature parameters for each sample (four repeats)

| Samples | Measured | | | | Calculated |
	a (µm)	b (µm)	h (µm)	L (µm)	ϕ_s
P1	22.9 ± 3.1	15.5 ± 1.7	67.0 ± 9.0	92	0.042 ± 0.007
P2	22.0 ± 2.9	21.3 ± 1.7	126.3 ± 6.5	107	0.041 ± 0.006
P3	56.5 ± 1.3	22.5 ± 2.4	66.8 ± 6.8	122	0.085 ± 0.009
P4	78.5 ± 1.4	55.8 ± 0.6	109.8 ± 5.1	142	0.217 ± 0.005
P5H	61.3 ± 0.8	37.8 ± 1.4	58.0 ± 0.4	141	0.067 ± 0.003
P6H	76.5 ± 1.4	74.8 ± 1.0	111.3 ± 1.4	164	0.123 ± 0.003
Gr1	21.0 ± 0.5	—	66.5 ± 1.0	92	0.228 ± 0.226
Gr2	13.9 ± 0.5	—	68.5 ± 1.2	107	0.130 ± 0.005

from the primary microfeatures; the hierarchical nature of the features are not taken into consideration. All features were designed to have different solid fraction, except for P1 and P2, where P2 can be considered a special case of a rectangular pillar structure, exhibiting in fact a square top.

3.2 Surface wettability

Table 2 presents the water contact angles on both the silanized and the non-silanized surfaces. Immediately after the laser micromachining process, the non-silanized samples were superhydrophilic. However, with time in the presence of CO_2, these samples became superhydrophobic, as explained elsewhere.[40]

The silanization process increased the dynamic contact angles (both the advancing, θ_A, and the receding, θ_R, contact angles) on the flat copper sample; however, the dynamic contact angles on both the silanized and the non-silanized laser-patterned samples were surprisingly similar. All contact angles on the silanized and the non-silanized laser-patterned surfaces were larger than 150°, and the hysteresis values were less than 10°. Moreover, we observed that the water droplet sat on a composite surface made of solid and air pockets for all samples, as shown exemplarily for sample P2 in Fig. 6. Thus, all our laser-patterned surfaces are classified as superhydrophobic. In addition, we submerged all samples in water to test for wetting robustness. All samples came out dry without any sign of water penetration in the features. In addition to the visual inspection, we deposited a 2 µL water droplet on the surface after
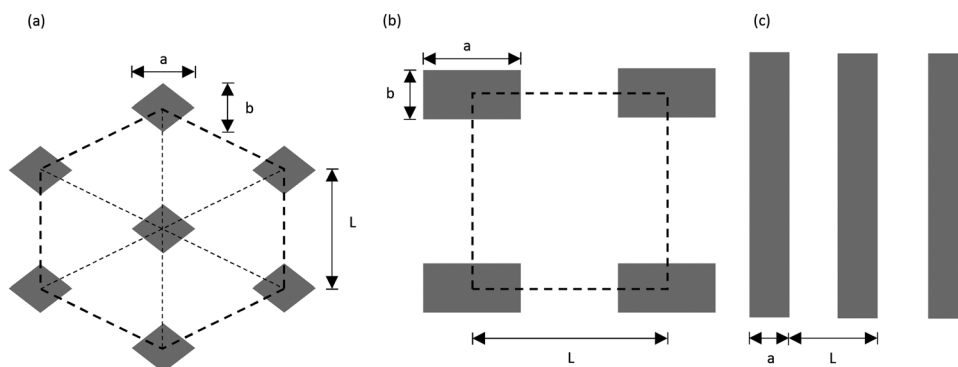
spots on the lased patch, whereas for laser-inscribed multiple scans, the surface structures grew outside of the effective beam diameter. The growth of the microfeatures at the edge of the inscribed lines can be attributed to the accumulation of laser pulses[39] and the re-deposition of nanoparticles.[30] Future investigations with different materials will need to elucidate the exact mechanism behind the laser-inscribed peripheral microstructure formation.

Primary feature size is one of the important parameters that affect the slip lengths on the surfaces. Fig. 5 illustrates the notation for the feature sizes (width, length, pitch) used in this work, and the respective dimensions, including the height (h) of the features, for all eight samples are listed in Table 1 along with the standard error of the mean (four measurements). The last column in Table 1 shows the calculated primary solid fraction (ϕ_s) for each sample. It is important to note that the reported solid fractions are merely the solid fractions calculated

Fig. 5 Top view of the characteristic dimensions of the features (a and b) and the pitch (L) for the (a) rhombic posts in a regular hexagonal arrangement, (b) rectangular posts in a square lattice arrangement, and (c) grates in a parallel arrangement.

Table 2 Dynamic water contact angles (three repeats) on silanized and non-silanized samples

Samples	θ_A (°)		θ_R (°)	
	Non-silanized	Silanized	Non-silanized	Silanized
Flat Cu	97 ± 3	113 ± 2	73 ± 6	105 ± 4
P1	162 ± 1	161 ± 1	157 ± 1	158 ± 1
P2	162 ± 1	162 ± 1	155 ± 1	155 ± 2
P3	160 ± 2	160 ± 1	153 ± 1	152 ± 1
P4	161 ± 1	161 ± 1	156 ± 1	156 ± 1
P5H	158 ± 1	153 ± 2	157 ± 1	150 ± 3
P6H	157 ± 2	156 ± 2	154 ± 2	152 ± 2
Gr1	160 ± 1	161 ± 1	156 ± 2	160 ± 1
Gr2	158 ± 1	158 ± 2	156 ± 1	157 ± 1
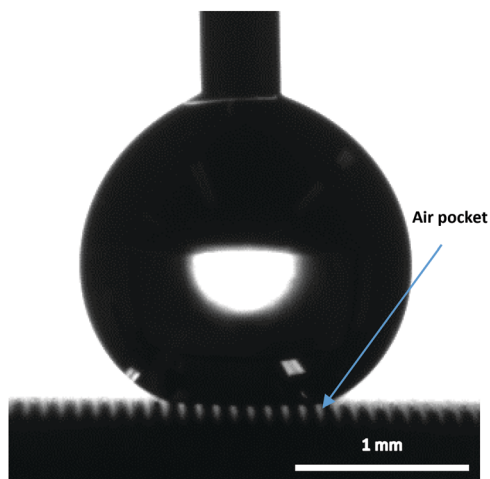
Fig. 6 Water droplet sitting on sample P2.

removing the sample from the water. The water droplet rolled off without spreading on the surface. Thus, the robustness of the surfaces, in terms of the Cassie wetting state, was established up to a pressure of 4 kPa.

3.3 Slip lengths on different surface patterns

Fig. 7 shows the measured slip lengths on all eight silanized samples. The overall mean slip length is the average of the mean slip lengths at nine different shear rates (each with 4 repeats). The micro/nano structures generated during laser micromachining did not dislodge due to the exerted shear stress as can be seen from the reproducible nature of the slip lengths in successive runs. As the effect of shear rate on slip lengths is still debated,[8,24,41] we chose to use the slip lengths at a defined shear rate to compare different samples. Our choice was further supported from a statistical analysis (paired Student's t-test), as we have found no statistically significant differences between the overall mean slip lengths and the mean slip lengths at 110 s^{-1} shear rate among all samples (statistical parameters are presented in Table S1 in ESI†). Thus, we used the average slip lengths at 110 s^{-1} for all subsequent comparative analysis. For the interested reader, the variations of slip length as a function of shear rate on different samples are shown in Fig. S2–S5 in ESI.†
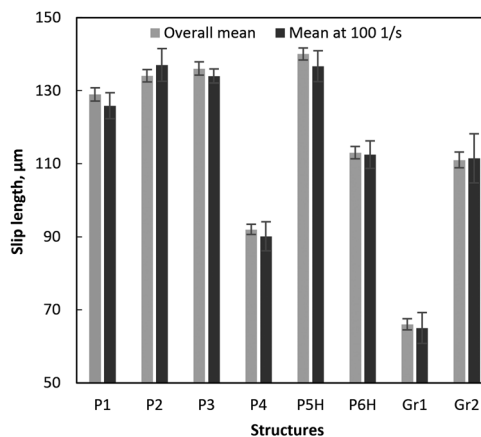

Fig. 7 Overall mean slip lengths and mean slip lengths at 100 s^{-1} shear rate for the silanized samples.

Fig. 8 plots the normalized slip lengths (effective slip length per pitch of the arrangement) against the solid fraction of the samples. Moreover, the plotted curves represent the theoretical prediction for grates arranged in the direction of flow[42–44] and the prediction resulting from an experimental model for posts arranged in a square lattice.[32] We observed 36–65% higher slip lengths on posts arranged in a square lattice than what was measured in the previous study by Lee and Kim (2008).[32] Similarly, our slip lengths on grates were up to 111% higher compared to the slip lengths from the theoretical prediction of Philip (1972).[43,44] However, the general trend of increasing normalized slip lengths with decreasing solid fractions for grates and posts (arranged in a square lattice) matches with the theoretical and the previous experimental model, respectively. Although no analytical model or previous experimental results are available for the hexagonal arrangement, the increase in normalized slip lengths with decreasing solid fraction was also observed for the posts arranged in that manner. However, the hexagonal arrangement resulted in a lower normalized slip length compared to the other two arrangements.

The increase in effective slip lengths with decreasing solid fraction was predicted by Ybert *et al.* (2007) with a scaling and a
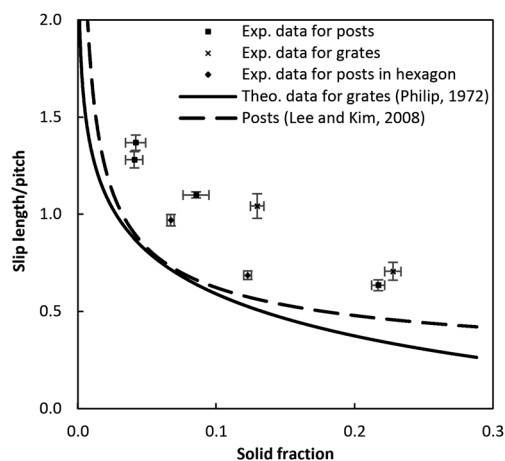
Fig. 8 Normalized slip lengths as a function of solid fraction.

numerical analysis.[6] Later, other researchers proposed mathematical relations for posts arranged in a square lattice derived by a semi-analytical method[45] and an analytical method.[46] All these mathematical relations produced very close slip length values with an error up to 4%. However, Lee and Kim (2008) experimentally found that the aforementioned relations do not hold for a fluid rotating in a cone-and-plate rheometer on circular posts arranged in a square lattice as the flow direction changes continuously with respect to the posts arrangement.[32] Thus, they proposed a modified relation for the slip lengths on post structures by linearly fitting their experimental results.[10]

$$\frac{\delta}{L} = \left(\frac{m}{\sqrt{\phi_s}} + n \right) \qquad (2)$$

Here δ is the effective slip length, L is the pitch, ϕ_s is the solid fraction, m and n are the fitting parameters with the values of 0.1555 and 0.132, respectively. We compared our measured slip lengths on post structures arranged in a square lattice to the slip lengths calculated using this equation. Both Lee and Kim's work and our present work dealt with posts arranged in a square lattice. However, the previous study used circular posts, whereas our study is based on rectangular posts. Yet, we claim that the difference in post shapes is not the reason for the higher slip lengths observed in our study. To the best of our knowledge, the effect of post shape on slip lengths was not studied experimentally. However, theoretical models exist for predicting the slip lengths on both circular and square posts, which indicate that the slip lengths on circular posts are slightly higher than those on the square posts.[45] For example, for a solid fraction of 0.041 and a pitch of 107 μm (similar to sample P2), the increase in slip length on circular posts will be only 3.5% compared to square posts. Thus, the circular post analysis can readily be used as a valid approximation in a square pillar analysis. However, sample P2 in our study, which is a square post sample, showed a 42% increase in slip length compared to the previous study with circular posts. Thus, we conclude that the large differences in slip lengths are not due to the post shape.

However, we hypothesize that the hierarchical structures contributed to the increase in slip lengths. An increase in slip length was observed for nanostructures on top of the original posts in other studies.[12,27] These hierarchical surfaces increase the overall effective slip length of the samples as the nanostructures themselves act as the intrinsic slip surfaces. In our study, the secondary micro-columns acted as the intrinsic slip surface. In addition, the tertiary nanostructures might contribute to the intrinsic slip length on the micro-columns. It is almost impossible to quantify the increase in slip lengths on the laser-induced three-tier hierarchical feature because of the irregular arrangements of the hierarchical features. However, here we will present a very rough estimate of slip length enhancement to verify that the increase in slip lengths can indeed be attributed to the effect of surface hierarchy. Sample P3 has comparatively homogeneous secondary microfeatures on it; thus, we chose this sample for the estimation. We estimated

the average micro-column feature sizes from confocal microscopy images. The diameter of the micro-columns varied from 4–10 μm. The pitch between the micro-columns varied widely from 8–17 μm. For a conservative estimate, we will use a 6 μm column with 12 μm pitch in the following calculation. Furthermore, we assumed a square arrangement of the micro-columns (illustrated in Fig. S6 of the ESI†). By using eqn (2), it is possible to estimate the intrinsic micro-slip caused by our micro-columns on top of the primary post features. The estimated micro-slip is about 3.7 μm. It is obvious that if there is an intrinsic micro-slip on the solid–liquid contact area of a patterned sample, then this micro-slip will enhance the effective slip length, and the enhancement will be a function of the primary solid fraction of the sample. By using this micro-slip length, the increase in slip length ($\Delta\delta$) is calculated following considerations outlined in the work of Ng and Wang (2010):[45]

$$\Delta\delta = \delta_\lambda - \delta_0 \cong \frac{\lambda}{\phi_s} \qquad (3)$$

where δ_λ is the effective slip length for a patterned surface that has a primary solid fraction of ϕ_s and an intrinsic micro-slip (λ) on top of the primary features, δ_0 is the effective slip length for the same patterned surface without the intrinsic micro-slip. This increase in slip length was compared to the predicted slip length computed by using eqn (2) for a non-hierarchical surface with a similar post geometry. For sample P3, with the estimated micro-slip of 3.7 μm, we calculated a 43 μm (47%) increase in the slip length, whereas experimentally 53 μm increase in slip length was observed in our study. This estimation only takes into account the effect of micro-columns. However, the nanostructures on top of the micro-columns can also increase the intrinsic slip on the micro-columns. The closeness of our estimated increase in slip length to the experimentally observed increase in slip length supports our hypothesis that micro-slip on the micro-columns contribute significantly to the overall drag reduction.

In the following, we extend the argument of intrinsic slip on top of the primary features to our grate samples arranged in the direction of flow. Philip (1972) developed a model for predicting the slip length on a parallel grate sample:[43,44]

$$\delta = -\frac{L}{\pi} \ln \left(\cos \left(\frac{\pi(1 - \phi_s)}{2} \right) \right) \qquad (4)$$

We compared our measured slip lengths on parallel grates to the slip lengths calculated using this equation. Although our measured slip lengths vary widely from the theoretical prediction, here we will show that the trend of increasing slip length with decreasing solid fraction still follows this theoretical prediction accurately. First, we assume that the intrinsic slip is alike (δ_0) for both grate samples (Gr1 and Gr2). We based this assumption on the similarity between the secondary features of both samples as can be seen from the SEM images of Fig. 2(a) and (b). Gr1 and Gr2 grate samples have slip length enhancements (difference between the theoretical prediction and the experimental results) of 31 μm ($\Delta\delta_1$) and 54 μm ($\Delta\delta_2$) respectively. The ratio between the slip length enhancements is 0.57 ($\Delta\delta_1/\Delta\delta_2$). By using equal intrinsic slip lengths and different solid fractions for both the

samples in eqn (3), we get an enhancement ratio of 0.57 ($\Delta\delta_1/\Delta\delta_2 = \phi_{s2}/\phi_{s1}$).

Unlike the square lattice and parallel grate arrangement, we were unable to estimate the slip length enhancement induced by the hierarchical roughness for the hexagonal geometry because of the lack of any theoretical model. Thus, more research needs to be performed on non-hierarchical posts arranged in a hexagonal lattice to confirm our results obtained on the hierarchical surfaces.

Overall, we conclude that the experimental results for our rectangular post and grate samples support the respective theoretical predictions if we attribute the slip length enhancement to the hierarchical nature of the sample.

3.4 Slip lengths on samples with different surface chemistry

The slip lengths observed on non-silanized and silanized samples are shown in Fig. 9. We found statistically significant differences in slip lengths for samples P1, P2, P3, and P5H. The test statistics and the relevant parameters are presented in the ESI† (Table S2). Sample P6H is not included in Fig. 9, as we could not confidently determine the slip length on the non-silanized P6H sample. The sample was not homogenously hydrophobic likely due to contamination from the environment. For all sample pairs the silanized surface shows a higher mean slip length compared to the respective non-silanized surface.

We attribute the difference in slip lengths to the difference in surface chemistry. The intrinsic contact angles on the flat silanized and the non-silanized samples were not similar. The flat silanized copper sample had higher dynamic contact angles and lower hysteresis compared to the flat non-silanized sample (Table 2). The surface energies are different for the silanized and the non-silanized samples as indicated by the different contact angles measured on the flat surfaces. Thus, we expect a different behaviour from the patterned silanized and the non-silanized surfaces. Surprisingly, the dynamic contact angles on the patterned silanized and the non-silanized surfaces were similar. Thus, we argue that the contact angles we measured on the patterned samples were not actual contact angles, rather

Fig. 9 Slip lengths comparison on silanized and non-silanized laser-patterned surfaces.

apparent contact angles. On a rough surface, the apparent contact angle is the angle between the hypothetical flat surface and the tangent of the liquid–gas interface at the triple line. Moreover, the actual contact angle is not measurable on a rough surface with the current state of measurement techniques.[5,47] Thus, the differences, if any, in actual contact angles between the two types of the samples were not observed in goniometer measurements. Fortunately, other indirect measurements, such as that of the penetration depth, can confirm that different actual contact angles are indeed present on these two types of surfaces. The air–water interface hanging between surface features is not flat, and the depth of penetration (distance from the top of the feature to the lowest point of the air–water interface) depends on the surface chemistry at the anchoring points and the applied pressure. We measured the depth of the air–water interface for both types of the samples. Under equal pressure application, we measured deeper depth of the air–water interface on the non-silanized sample compared to the depth of the interface on the silanized sample, which is shown exemplarily for sample P4 in Fig. 10. The non-silanized surface shows 7.3 ± 0.3 μm penetration depth, whereas the silanized sample shows 5.3 ± 0.3 μm (3 repeats) penetration depth. As the applied pressure was alike on both the surfaces and the surface structure did not significantly change with the coating process (Fig. 10(d) and (e)), the difference in the penetration depths is the result of the difference in surface chemistry on these two types of the surfaces.

The difference in penetration depths on these two surfaces can be manifested by sagging, de-pinning, or both mechanisms. With increasing pressure the air–water interface can sag and de-pin to different extent dictated by the actual contact angles. In addition, the de-pinning behaviour is more likely to occur when the surface features are not sharp at the edge,[27] as is the case for our surface structures. In the case of de-pinning the triple line will move down the feature walls, which results in an increased solid fraction and reduced slip lengths. Therefore, we can conclude that the comparatively lower slip lengths on the non-silanized surfaces were due to the difference in chemistry of the surfaces.

To investigate further the effect of surface chemistry, we conducted a dynamic robustness test on both the silanized and the non-silanized surfaces. If a sufficiently high pressure is applied on an air–water interface the de-pinning and/or sagging mechanisms can result in a transition from the Cassie to the Wenzel wetting state.[5] For surfaces with different actual contact angles, this transition will not happen at the same pressure. In the flow channel water flowed on the samples for 5 minutes. After 5 minutes the surfaces were removed from the flow cell and observed with the naked eyes. The silanized surfaces were completely dry while the non-silanized surfaces were visibly wet, as the air–water interface had collapsed (Fig. 11). We also noticed that the air–water interface collapsed near the high-pressure zone in the channel, where the flow entered (from the left to the right in the figure). Therefore, the dynamic robustness test provides another proof that the difference in surface chemistry, which did not manifest itself in different measured contact angles, is responsible for the different slip length results on the surfaces of the same pattern type.
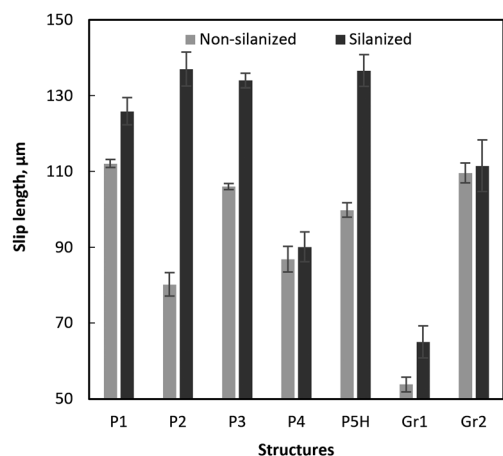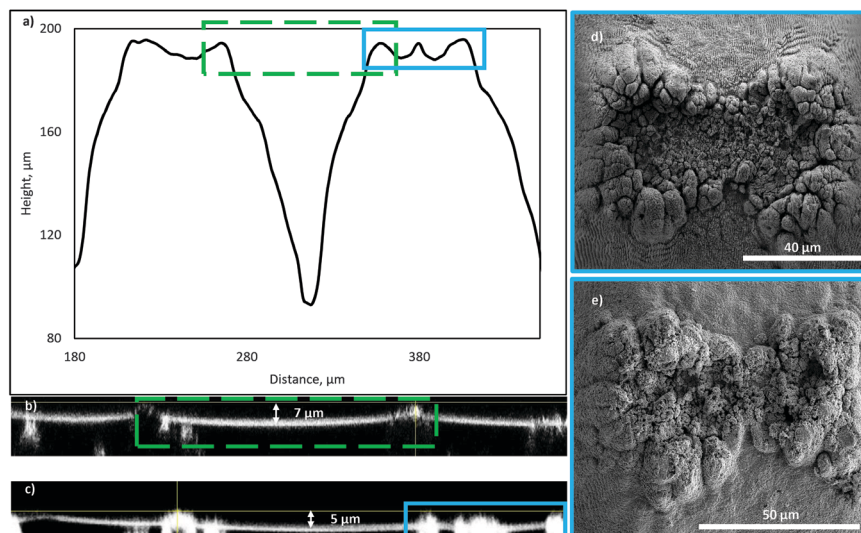
Fig. 10 (a) Area of interests for measuring the location of the air–water interface are indicated on the height profile of the sample P4; penetration depth for (b) non-silanized and (c) silanized P4 sample; and SEM images of (d) non-silanized and (e) silanized P4 sample.
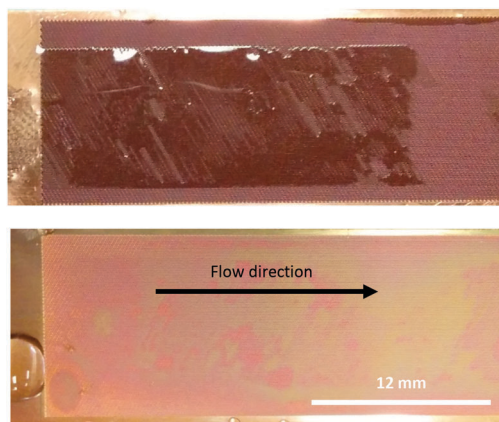

Fig. 11 Surfaces after testing in a flow channel, non-silanized P5H surface (top), and silanized P5H surface (bottom).

4. Conclusions

In this study we have successfully fabricated drag reducing hierarchical superhydrophobic surfaces in a single-step laser micromachining process. Instead of creating microfeatures superimposed with nanofeatures, we fabricated surfaces that have primary microfeatures superimposed with secondary microfeatures, which are again decorated with nano features. Thus, using a multiple laser scanning method we have effectively created a surface that has a tertiary level of roughness.

By using these surfaces we have observed considerably higher drag reduction than what was predicted from theoretical and experimental models on non-hierarchical surfaces. We confirmed this enhancement of drag reduction by considering the geometry of the secondary features in calculations. Thus, the intrinsic slip on the primary features was supported by the additional level of roughness.

Furthermore, we compared the drag reduction abilities of different arrangements of surface features, such as rectangular posts in a square lattice, grates parallel to the flow, and rhombic posts in a hexagonal lattice. While the latter facilitates a stable Cassie state, it nevertheless resulted in a lower normalized slip length compared to the other two arrangements at a fixed solid fraction.

We also tested the robustness of the patterned surfaces and verified the Cassie state of wetting for all samples through contact angle goniometry. While the contact angles were similar for both the silanized and the non-silanized samples, we observed higher slip lengths on the silanized samples, which we explained by a lower penetration depth. Thus, we showed that the surface chemistry plays a role in drag reduction even though it was not evidenced by the contact angles.

Our hierarchical drag-reducing surfaces have the potential to pave the way for larger-scale implementation considering the performance of the surfaces and the simplicity of the fabrication method.

Acknowledgements

Notes and references

1 J. P. Rothstein, *Annual Review of Fluid Mechanics*, Annual Reviews, Palo Alto, 2010, vol. 42, pp. 89–109.
2 D. Quere, *Annu. Rev. Mater. Res.*, 2008, **38**, 71–99.
3 R. S. Voronov, D. V. Papavassiliou and L. L. Lee, *Ind. Eng. Chem. Res.*, 2008, **47**, 2455–2477.
4 T. Lee, E. Charrault and C. Neto, *Adv. Colloid Interface Sci.*, 2014, **210**, 21–38.

5 E. Bormashenko, *Adv. Colloid Interface Sci.*, 2015, **222**, 92–103.

6 C. Ybert, C. Barentin, C. Cottin-Bizonne, P. Joseph and L. Bocquet, *Phys. Fluids*, 2007, **19**, 123601.

7 C. L. M. H. Navier, *Mem. Acad. Sci. Inst. Fr.*, 1823, **6**, 389–440.

8 C. H. Choi, K. J. A. Westin and K. S. Breuer, *Phys. Fluids*, 2003, **15**, 2897–2902.

9 D. C. Tretheway and C. D. Meinhart, *Phys. Fluids*, 2002, **14**, L9–L12.

10 C. Lee and C. J. Kim, *Langmuir*, 2009, **25**, 12812–12818.

11 J. Ou, B. Perot and J. P. Rothstein, *Phys. Fluids*, 2004, **16**, 4635–4643.

12 Y. C. Jung and B. Bhushan, *J. Phys.: Condens. Matter*, 2010, **22**, 035104.

13 A. Maali, Y. Pan, B. Bhushan and E. Charlaix, *Phys. Rev. E: Stat. Phys., Plasmas, Fluids, Relat. Interdiscip. Top.*, 2012, **85**, 066310.

14 D. Maynes, K. Jeffs, B. Woolford and B. W. Webb, *Phys. Fluids*, 2007, **19**, 093603.

15 R. J. Daniello, N. E. Waterhouse and J. P. Rothstein, *Phys. Fluids*, 2009, **21**, 085103.

16 T. Yamada, C. Hong, O. J. Gregory and M. Faghri, *Microfluid. Nanofluid.*, 2011, **11**, 45–55.

17 B. Woolford, D. Maynes and B. W. Webb, *Microfluid. Nanofluid.*, 2009, **7**, 121–135.

18 B. Woolford, J. Prince, D. Maynes and B. W. Webb, *Phys. Fluids*, 2009, **21**, 085106.

19 S. Srinivasan, W. Choi, K.-C. Park, S. S. Chhatre, R. E. Cohen and G. H. McKinley, *Soft Matter*, 2013, **9**, 5691–5702.

20 N. Kashaninejad, N.-T. Nguyen and W. K. Chan, *Phys. Fluids*, 2012, **24**, 112004.

21 D. Dilip, N. K. Jha, R. N. Govardhan and M. S. Bobji, *Colloids Surf., A*, 2014, **459**, 217–224.

22 P. Joseph, C. Cottin-Bizonne, J. M. Benoit, C. Ybert, C. Journet, P. Tabeling and L. Bocquet, *Phys. Rev. Lett.*, 2006, **97**, 156104.

23 M. Zhou, J. Li, C. C. Feng, C. X. Wu, R. Yuan and L. Cai, *Chem. Vap. Deposition*, 2010, **16**, 12–14.

24 M. Zhou, J. Li, C. X. Wu, X. K. Zhou and L. Cai, *Soft Matter*, 2011, **7**, 4391–4396.

25 M. A. Samaha, H. V. Tafreshi and M. Gad-el-Hak, *Phys. Fluids*, 2012, **24**, 112103.

26 G. D. Bixler and B. Bhushan, *Nanoscale*, 2014, **6**, 76–96.

27 C. Lee and C. J. Kim, *Langmuir*, 2011, **27**, 4243–4248.

28 H. Park, G. Y. Sun and C. J. Kim, *J. Fluid Mech.*, 2014, **747**, 722–734.

29 E. Aljallis, M. A. Sarshar, R. Datla, V. Sikka, A. Jones and C. H. Choi, *Phys. Fluids*, 2013, **25**, 025103.

30 A. Y. Vorobyev and C. L. Guo, *Laser Photonics Rev.*, 2013, **7**, 385–407.

31 S. Moradi, S. Kamal, P. Englezos and S. G. Hatzikiriakos, *Nanotechnology*, 2013, **24**, 415302.

32 C. Lee, C. H. Choi and C. J. Kim, *Phys. Rev. Lett.*, 2008, **101**, 064501.

33 K. Ahmmed, C. Grambow and A.-M. Kietzig, *Micromachines*, 2014, **5**, 1219–1253.

34 J. Lehr and A.-M. Kietzig, *Optics and Lasers in Engineering*, 2014, **57**, 121–129.

35 X. F. Gao, X. Yao and L. Jiang, *Langmuir*, 2007, **23**, 4886–4891.

36 B. J. Li, M. Zhou, R. Yuan and L. Cai, *J. Mater. Res.*, 2008, **23**, 2491–2499.

37 F. Gentile, M. L. Coluccio, N. Coppedè, F. Mecarini, G. Das, C. Liberale, L. Tirinato, M. Leoncini, G. Perozziello, P. Candeloro, F. De Angelis and E. Di Fabrizio, *ACS Appl. Mater. Interfaces*, 2012, **4**, 3213–3224.

38 E. J. Y. Ling, J. Saïd, N. Brodusch, R. Gauvin, P. Servio and A.-M. Kietzig, *Appl. Surf. Sci.*, 2015, **353**, 512–521.

39 P. T. Mannion, J. Magee, E. Coyne, G. M. O'Connor and T. J. Glynn, *Appl. Surf. Sci.*, 2004, **233**, 275–287.

40 A. M. Kietzig, S. G. Hatzikiriakos and P. Englezos, *Langmuir*, 2009, **25**, 4821–4827.

41 C. H. Choi and C. J. Kim, *Phys. Rev. Lett.*, 2006, **96**, 066001.

42 E. Lauga and H. A. Stone, *J. Fluid Mech.*, 2003, **489**, 55–77.

43 J. R. Philip, *Z. Angew. Math. Phys.*, 1972, **23**, 960–968.

44 J. R. Philip, *Z. Angew. Math. Phys.*, 1972, **23**, 353–372.

45 C. O. Ng and C. Y. Wang, *Microfluid. Nanofluid.*, 2010, **8**, 361–371.

46 A. M. J. Davis and E. Lauga, *J. Fluid Mech.*, 2010, **661**, 402–411.

47 A. Marmur, *Soft Matter*, 2006, **2**, 12–17.